

# InGaN/Si Double-Junction Photocathode for Unassisted Solar Water Splitting

Srinivas Vanka, Baowen Zhou, Rasha A. Awni, Zhaoning Song, Faqrul A. Chowdhury, Xuedong Liu, Hamed Hajibabaei, Wen Shi, Yixin Xiao, Ishtiaque A. Navid, Ayush Pandey, Rong Chen, Gianluigi A. Botton, Thomas W. Hamann, Dunwei Wang, Yanfa Yan, and Zetian Mi\*



Cite This: *ACS Energy Lett.* 2020, 5, 3741–3751



Read Online

ACCESS |



Metrics & More

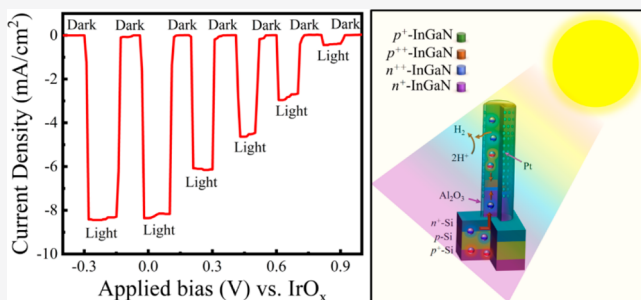


Article Recommendations



Supporting Information

**ABSTRACT:** Simultaneously achieving efficient and stable operation is a major challenge for developing sustainable and economical solar water-splitting systems. In this work, we demonstrate, for the first time, a monolithically integrated InGaN/Si double-junction photocathode, which can enable relatively efficient and stable unassisted solar water splitting. The device consists of a *p*-type InGaN top junction, which is monolithically integrated on a bottom Si *p*–*n* junction through a dislocation-free  $n^{++}/p^{++}$  InGaN nanowire tunnel junction. With the incorporation of Pt catalysts and a thin  $\text{Al}_2\text{O}_3$  surface passivation layer, a solar-to-hydrogen efficiency of  $\sim 10.3\%$  and stable operation of 100 h was measured in 0.5 M  $\text{H}_2\text{SO}_4$  in a two-electrode configuration for unbiased photoelectrochemical water splitting. Significantly, such an efficient and stable water-splitting device is achieved using the two most produced semiconductors, i.e., Si and Ga(In)N, promising large-scale implementation of efficient, stable, and low-cost solar hydrogen production systems.



Solar hydrogen ( $\text{H}_2$ ) fuel is one of the best sustainable and clean alternatives to address the increasing global energy demand by using the two most abundant natural resources on earth, i.e., water and sunlight.<sup>1–3</sup> Photoelectrochemical (PEC) water splitting is one of the most promising approaches for solar hydrogen production.<sup>3–5</sup> For this approach to be competitive, it is pertinent to achieve solar-to-hydrogen (STH) efficiency  $>10\%$ , lifetime stability  $>10$  years, and low  $\text{H}_2$  production costs.<sup>2,6,7</sup> PEC devices using a tandem configuration, with a top light absorber band gap of  $\sim 1.8$  eV and bottom light absorber band gap of  $\sim 1.1$  eV, have the potential to reach a maximum theoretical STH efficiency of  $\sim 30\%$ .<sup>3,7–9</sup> Apart from the energy band gap requirements, a tandem device must have a functional tunnel junction (TJ), which needs to be optically transparent, electrically conducting, and possess a low level of structural defects and dislocations. Since the first demonstration of a tandem water-splitting device by Khaselev et al. using III–V semiconductors,<sup>10</sup> significant progress has been made in unassisted PEC water splitting for solar-hydrogen production in the past two decades. The state-of-the-art STH efficiency and stability reported for some of these photoelectrodes is summarized in Figure 1a. Although STH efficiency values up to 19% have been reported,<sup>9–13</sup> they suffer from several critical issues, including (i) poor stability due to their inherent spontaneous photocorrosion and oxidation in acidic or alkaline

electrolytes<sup>14,15</sup> and (ii) high costs associated with the large area III–V substrates.<sup>6</sup> Significant efforts have been devoted to improving the stability of III–V water-splitting devices, including the incorporation of a  $\text{TiO}_2$  surface protection layer<sup>11</sup> and the bifacial electrode design with thick metal layers for GaAs photoelectrodes.<sup>13</sup> These approaches, however, have limited success and often lead to significantly reduced STH efficiency. Illustrated in Figure 1a, even with various surface protection schemes, the stability of III–V water-splitting devices is still low ( $<40$  h) when measured in practical two-electrode conditions. On the other hand, as seen in Figure 1a, tandem photoelectrodes based on non-III–V materials, e.g., Si<sup>16</sup> and metal oxides such as  $\text{BiVO}_4$  and  $\text{Fe}_2\text{O}_3$ ,<sup>17–20</sup> are often plagued by very low STH efficiencies, in addition to limited stability.<sup>21–23</sup> There is, therefore, an urgent quest for semiconductor photoelectrodes that are intrinsically stable, can be

Received: July 23, 2020

Accepted: October 29, 2020

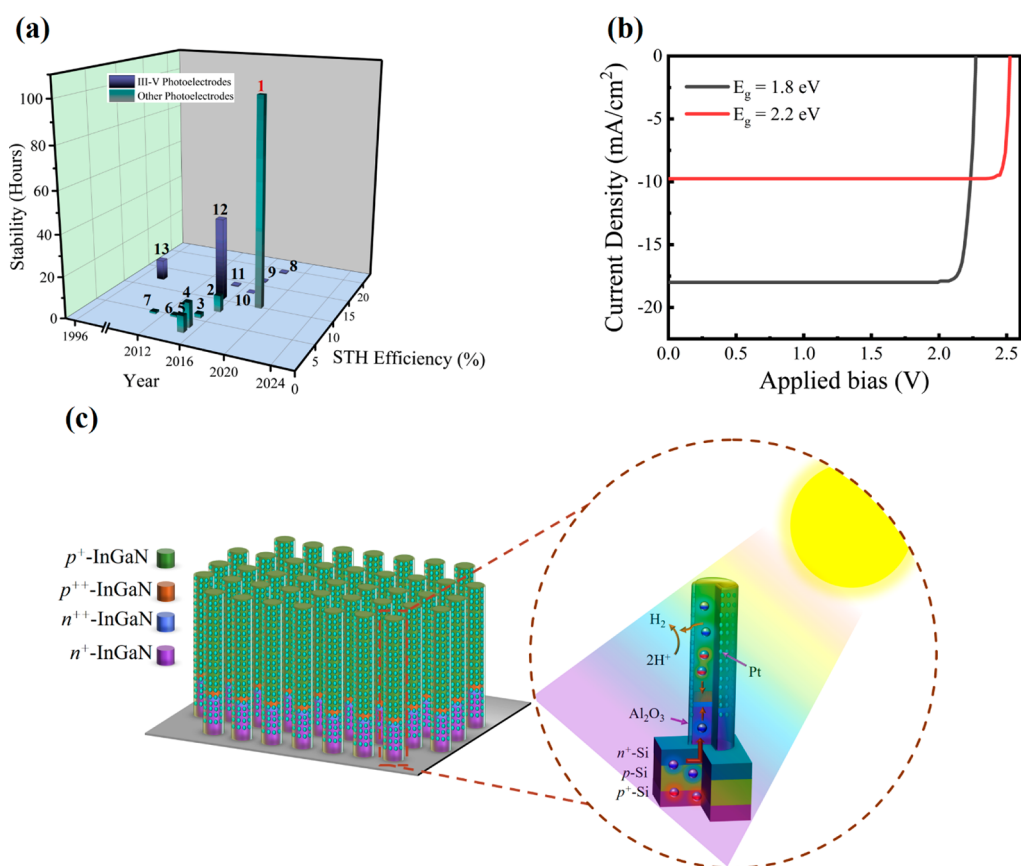


**Figure 1.** Comparison of state-of-the-art photoelectrodes and design and performance prediction of InGaN/Si double-junction photocathode. (a) Graphical representation of stability and solar-to-hydrogen (STH) efficiency for previously reported semiconductor photoelectrodes measured under AM 1.5G one sun illumination. Non-III–V semiconductor photoelectrodes: 1, this work; 2, BiVO<sub>4</sub>/Fe<sub>2</sub>O<sub>3</sub>/Si photoanode;<sup>20</sup> 3, WO<sub>3</sub>/BiVO<sub>4</sub> photoanode;<sup>19</sup> 4, Co–Ni dual doped BiVO<sub>4</sub>/I<sub>2</sub> perovskite photoanode;<sup>18</sup> 5, Co–Pi Mn-doped Fe<sub>2</sub>O<sub>3</sub>-I<sub>2</sub> perovskite photoanode;<sup>62</sup> 6, Co–Pi Gradient W:BiVO<sub>4</sub>/a:Si photoanode;<sup>17</sup> and 7, 3J a-Si Co/NiMoZn photoanode.<sup>16</sup> III–V semiconductor photoelectrodes: 8, Rh–TiO<sub>2</sub>–GaInP–GaInAs photocathode;<sup>12</sup> 9, PtRu–GaInP/GaInAs photocathode;<sup>9</sup> 10, Pt-metal/n<sup>+</sup>p GaAs and IrO<sub>x</sub>-metal/p<sup>+</sup>n GaAs;<sup>13</sup> 11, Rh/AlInP–GaInP/GaInAs photocathode;<sup>68</sup> 12, Ni–TiO<sub>2</sub>/GaInP/GaAs photoanode;<sup>11</sup> and 13, Pt/GaInP<sub>2</sub>/GaAs photocathode.<sup>10</sup> (b) Theoretical *J*–*V* simulation of an ideal In<sub>0.46</sub>GaN<sub>0.54</sub>/Si (black curve) and In<sub>0.32</sub>GaN<sub>0.68</sub>/Si (red curve) tandem photocathode under AM 1.5G one sun illumination. (c) Schematic of InGaN nanowire arrays on Si substrate after Pt and Al<sub>2</sub>O<sub>3</sub> deposition. The right side schematic is the cross-sectional view of nanowire and Si substrate showing light absorption by the p<sup>+</sup>-InGaN and Si, subsequent electron transfer from Si wafer to n<sup>+</sup>-InGaN, charge carrier recombination in the tunnel junction, and proton reduction on Al<sub>2</sub>O<sub>3</sub>/Pt-covered p<sup>+</sup>-InGaN nanowires.

manufactured at low cost and have a tunable energy band gap for efficient tandem water-splitting devices.

In this context, III-nitride semiconductors, i.e., Ga(In)N, have emerged as one of the most promising materials for next-generation semiconductor photoelectrodes.<sup>24–29</sup> They exhibit tunable direct band gap from 0.65 eV (InN) to 3.4 eV (GaN)<sup>30</sup> and have large carrier mobility<sup>24</sup> and high light absorption coefficient.<sup>31</sup> As such, III-nitrides have been intensively studied for PEC water splitting<sup>25–28</sup> as well as for other artificial photosynthesis devices.<sup>29,32–34</sup> Recently, it has been discovered that the surfaces of III-nitride nanostructures can be engineered to be N-rich, not only for their top *c*-plane but also for their nonpolar sidewalls, which can protect against photocorrosion and oxidation<sup>35,36</sup> and are stable in various electrolytes.<sup>34,36,37</sup> Moreover, such N-terminated III-nitride nanostructures can be grown directly on Si wafer without the formation of extensive dislocations, providing distinct opportunities to realize Si-based double-junction PEC water-splitting devices with a nearly ideal energy band gap configuration,<sup>7</sup> i.e., ~1.1 and 1.8 eV for the bottom Si and top In<sub>0.46</sub>GaN<sub>0.54</sub>N junction, respectively. Illustrated in Figure 1b is the simulated *J*–*V* characteristics for such a double-junction device, which can exhibit a maximum

photocurrent density of ~18 mA/cm<sup>2</sup> and photovoltage ~2.2 V under AM1.5G one sun illumination (see Table T1 for details about the calculation). To date, however, such an InGaN/Si double-junction PEC device has not been realized for unassisted PEC water splitting, partly limited by the lack of a defect-free tunnel junction that can integrate the top InGaN light absorber with the bottom Si p–n junction. In addition, the performance of such nanostructured PEC water-splitting devices suffers from surface recombination of photogenerated charge carriers<sup>15,23</sup> and the poor adhesion of photocatalyst nanoparticles on semiconductor surfaces.<sup>15,25,37,38</sup>

In this work, we have overcome these critical challenges and demonstrated, for the first time, an InGaN/Si double-junction device for unassisted PEC solar water splitting, which is achieved by utilizing a defect-free n<sup>+</sup>–InGaN/p<sup>+</sup>–InGaN nanowire tunnel junction to monolithically integrate the top N-terminated p<sup>+</sup>-InGaN light absorber with the underlying Si p–n junction. Moreover, an ultrathin Al<sub>2</sub>O<sub>3</sub> surface passivation layer is uniformly deposited on InGaN nanowire surfaces by atomic layer deposition (ALD), which significantly reduces surface recombination of photogenerated charge carriers and further helps stabilize Pt catalyst nanoparticles. A tandem PEC device

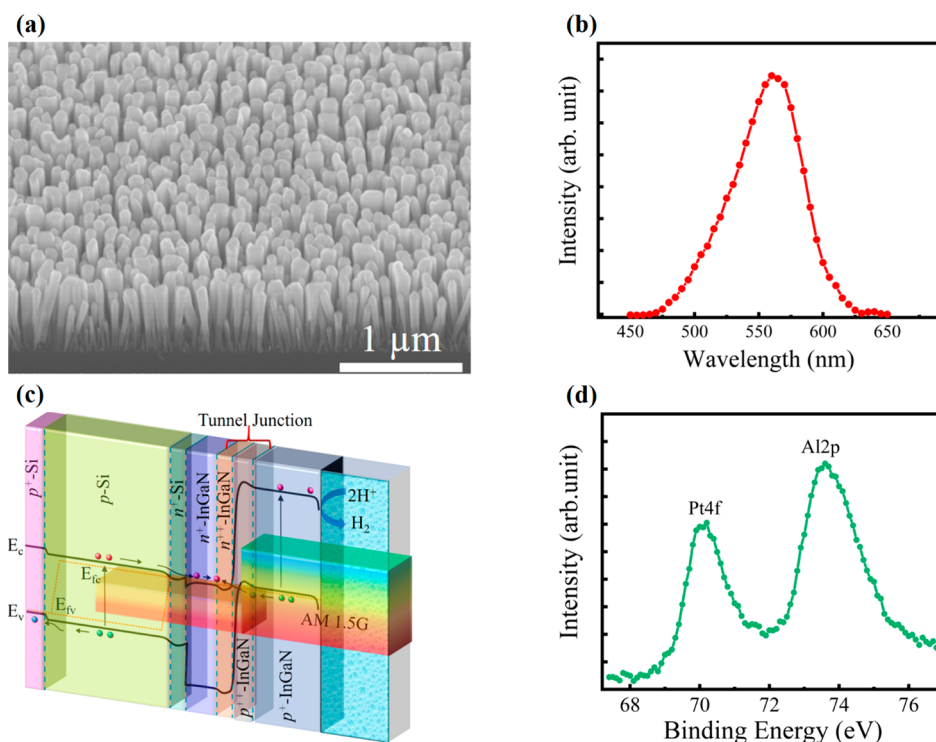


**Figure 2.** Structural and optical properties of as grown and surface-modified InGaN nanowires. (a) 45° tilt SEM image of as-grown  $p^+$ -InGaN nanowires with tunnel junction on Si wafer. (b) Room-temperature photoluminescence spectrum of as-grown  $p^+$ -InGaN nanowires from the best PEC performing region of the wafer (see Section S2). (c) Band-diagram of the  $p^+$ -InGaN/TJ/ $n^+$ - $p$  Si photocathode showing charge carrier generation in Si and  $p^+$ -InGaN, and charge extraction from  $p^+$ -InGaN. The top  $p^+$ -InGaN subcell (best PEC performing region) absorbs photons with  $h\nu \approx 2.2$  eV, or higher, and bottom Si subcell absorbs photons passing through the top subcell but with  $h\nu$  greater than the band gap of Si. The band diagram was drawn assuming nearly constant In incorporation throughout the nanowire. (d) XPS measurements of  $\text{Al}_2\text{O}_3/\text{Pt}/p^+$ -InGaN/TJ nanowires/ $n^+$ - $p$  Si photocathode for Pt 4f and Al 2p.

consisting of a top  $p^+$ -InGaN cell with an energy band gap of  $\sim 2.2$  eV shows  $V_{\text{on}} \approx 0.7$  V vs  $\text{IrO}_x$  and photocurrent density of  $\sim 8.4$   $\text{mA}/\text{cm}^2$  at 0 V vs  $\text{IrO}_x$  under AM 1.5G one sun illumination in 0.5 M  $\text{H}_2\text{SO}_4$ , with STH  $\approx 10.3\%$ . Chronoamperometry analysis for the photocathode shows stable operation for 100 h without any performance degradation for unassisted water splitting. Further impedance studies reveal the charge-transfer mechanism in the double-junction device. Given that Si and Ga(In)N, the two most produced semiconductors, can be manufactured at large scale with relatively low cost, this work provides a new approach for developing high-efficiency and high-stability PEC water splitting for solar  $\text{H}_2$  production.

As shown in Figure 1c, the double-junction photocathode (see Supporting Information Section S1) consists of  $p^+$ -InGaN top light absorber,  $p^+$ -InGaN/ $n^+$ -InGaN tunnel junction, and  $n^+$ - $p$  Si bottom light absorber. The  $n^+$ - $p$  Si wafers were prepared using thermal diffusion, and the details are described elsewhere.<sup>25</sup> The scanning electron microscopy (SEM) image, illustrated in Figure 2a, shows the nanowires are vertically aligned on  $n^+$ - $p$  Si wafer with diameters of  $\sim 80$  nm and lengths of  $\sim 600$ – $700$  nm. We have performed extensive studies on the growth of InGaN nanowires on Si<sup>24,33,34</sup> and found that PEC devices with the incorporation of an InGaN top cell with an average indium composition of  $\sim 32\%$  and an energy band gap of  $\sim 2.2$  eV provide the best PEC performance in this study. The photoluminescence (PL) emission spectrum (see Figure 2b) of the best PEC performing region, shows a strong peak emission at  $\sim 560$  nm (see Supporting Information Section S2 for more details on indium variation across the wafer), corresponding to

an energy band gap of 2.2 eV. The broad spectral line width also indicates significant indium compositional fluctuations from nanowire to nanowire, or within the same nanowires. Given the conduction band edge of  $\text{In}_{0.32}\text{Ga}_{0.68}\text{N}$  ( $\sim -0.5$  V vs RHE at pH 0<sup>30,39,40</sup>), photoexcited electrons from  $p^+$ -InGaN can, in principle, reduce protons without any external bias.<sup>32,33</sup> Additionally, it is important to note that previous studies confirmed the conduction band edges of GaN and Si are near-perfectly aligned,<sup>25</sup> which enables efficient transfer of photoexcited electrons from the underlying Si light absorber to the top  $p^+$ -InGaN. This unique property, together with the large surface area and light scattering and trapping of nanowires, is essential to achieve high-efficiency InGaN/Si double-junction photoelectrodes by significantly improving the charge carrier extraction (see Figure 1c) as well as light absorption.<sup>25</sup> The photogenerated electrons from  $n^+$ - $p$  Si wafer are extracted by  $n^+$ -InGaN nanowire arrays as shown in the inset of Figure 1c. Also shown in Figure 2c, the downward band bending of  $p^+$ -InGaN can promote the extraction of photogenerated electrons to the electrolyte. Additionally, because of the large valence band offset between  $n^+$ -InGaN and Si, the bottom  $n^+$ -InGaN acts as an active hole-blocking layer for  $n^+$ - $p$  Si to effectively suppress surface recombination. Photogenerated electrons from the bottom Si cell recombine with the photogenerated holes from the top  $p^+$ -InGaN layer in the TJ (as shown in Figures 1c and 2c). In this study, instead of forming the TJ directly on Si, we incorporate it on top of the bottom  $n^+$ -InGaN segment. This is because TJ incorporated in a nanowire segment has significantly fewer defects and dislocations<sup>41,42</sup> compared to direct integration on Si substrate, because of the lattice mismatch between InGaN and



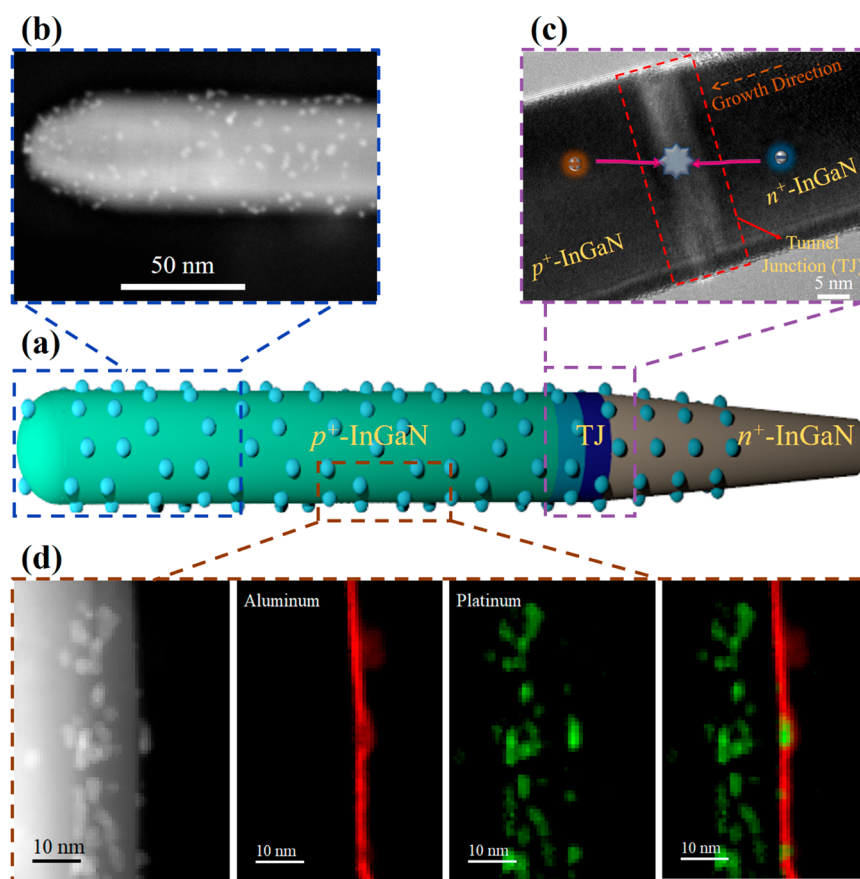


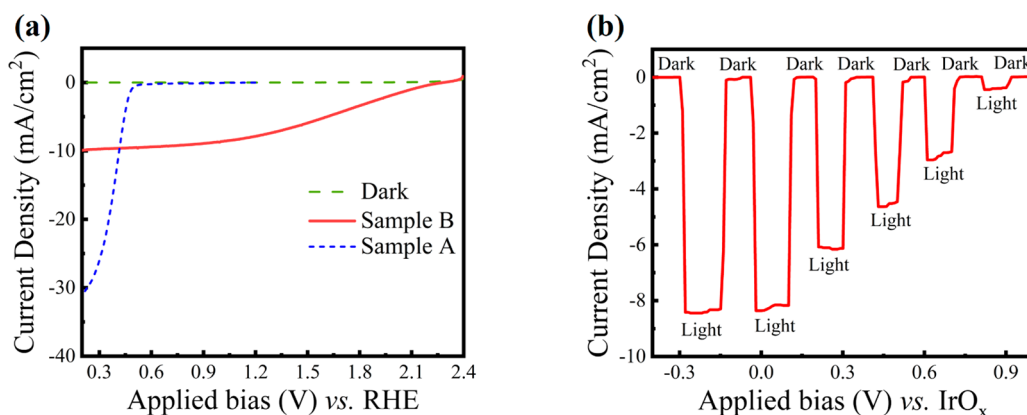
**Figure 3.** Structural characterization of surface-modified InGaN nanowire. (a) Schematic of single nanowire with Pt and  $\text{Al}_2\text{O}_3$ . (b) STEM-HAADF image of top  $p^+$ -InGaN segment (dark blue dashed box region in panel a). (c) Bright Field STEM image of tunnel junction region (pink dashed box region in panel a). The photogenerated holes (brown) from top  $p^+$ -InGaN and electrons (blue) from bottom  $n^+$ -InGaN/Si recombine in the tunnel junction indicated by the red dashed box in panel c. (d) STEM-HAADF and EELS elemental mapping showing Pt and  $\text{Al}_2\text{O}_3$  on the nanowire sidewall (brown dashed box region in panel a). The green/red image represents the combined color-coded Al (red) and Pt (green) maps.

Si. Previously, we have also demonstrated that defect-free Ga(In)N nanowires can significantly enhance the performance of single-junction Si photocathode.<sup>25,37,43</sup> To elucidate the role of TJ and top  $p^+$ -InGaN on the double-junction performance, we use  $n^+$ -InGaN nanowires/Si single-junction photocathode as a control sample in this study.

Before PEC testing,  $p^+$ -InGaN/TJ/ $n^+$ -p Si photocathode undergoes two-step surface modification as shown in Figure 1b. In the first step, Pt nanoparticles are deposited on  $p^+$ -InGaN/TJ/ $n^+$ -p Si using photodeposition (see Supporting Information Section S1). To further reduce the charge-transfer losses due to the surface recombination, it is pertinent to deposit passivation layer.<sup>44</sup> In the second step of surface modification, as shown in the inset of Figure 1c, the Pt nanoparticles/ $p^+$ -InGaN/TJ/ $n^+$ -p Si photocathode is covered by a thin layer of  $\text{Al}_2\text{O}_3$  (see Supporting Information Section S1). Although  $\text{Al}_2\text{O}_3$  is amphoteric, studies have shown that  $\text{Al}_2\text{O}_3$  can be stable in PEC reactions.<sup>45–47</sup> In previous reports, it was observed that  $\text{Al}_2\text{O}_3$ , which is a conductive transparent oxide layer, acts as a passivation layer for photoelectrodes.<sup>44–46</sup> This passivation layer not only protects the photoelectrode against oxidation in the electrolyte<sup>46,48</sup> but also enhances the overall reaction kinetics by reducing surface recombination.<sup>45,46</sup> Recently, metal–organic chemical vapor deposition (MOCVD) grown Ga-terminated  $n$ -GaIn epilayers with  $\text{Al}_2\text{O}_3$  protection layer ( $\sim 1$ – $2$  nm) showed enhanced stability and reduced over-

potential under water oxidation conditions.<sup>48</sup> The effect of a thin  $\text{Al}_2\text{O}_3$  passivation layer in reducing charge carrier-transfer resistance and providing better stability is discussed in the following paragraphs. The X-ray photoelectron spectroscopy (XPS) results of samples after surface modifications are shown in Figure 2d. The Pt 4f and Al 2p have peak positions at 70.2 and 73.9 eV, respectively, which correspond to metallic Pt peak<sup>49</sup> and  $\text{Al}_2\text{O}_3$  peak.<sup>50,51</sup>

Structural properties of the samples were further characterized using SEM (see Figure S3) and scanning transmission electron microscopy (STEM). Figure 3a shows the schematic representation of a single  $p^+$ -InGaN/TJ nanowire with Pt nanoparticles and  $\text{Al}_2\text{O}_3$  passivation layer. The STEM high-angle annular dark field (HAADF) image in Figure 3b shows that the top segment of the  $p^+$ -InGaN nanowire (blue box region in Figures 3a) has a diameter of  $\sim 80$  nm with Pt nanoparticle (size  $\sim 2$ – $3$  nm) coverage. The tunnel junction region of the nanowire is identified in Figure 3c. It is to be noted that the  $p^+$ -InGaN/ $n^+$ -InGaN tunnel junction is essential to enable recombination of photogenerated charge carriers<sup>52–54</sup> between the top  $p^+$ -InGaN subcell and bottom Si subcell without significant ohmic loss, thereby producing sufficient open-circuit potential (to be discussed in subsequent paragraphs) for unassisted water splitting. Furthermore, in Figure 3d, the nanowire sidewall is analyzed using electron energy loss spectroscopy (EELS) mapping. The STEM-HAADF image in



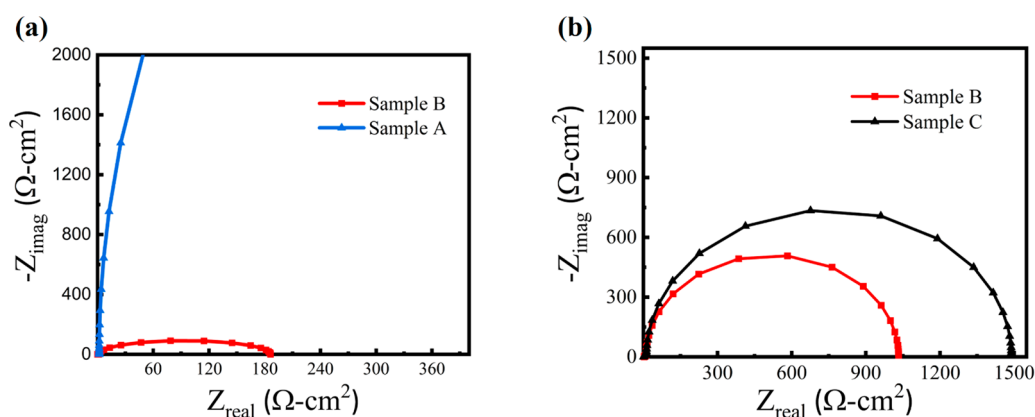
**Figure 4.** Photoelectrochemical performance of surface-modified InGaN/Si double-junction photocathode. (a) Three-electrode linear scan voltammogram (LSV) of sample B (red curve) and sample A (dotted blue curve) in 0.5 M  $\text{H}_2\text{SO}_4$  under AM 1.5G one sun illumination and dark conditions (dashed green curve) scan range between 2.4 and 0.3 V vs RHE. (b) Two-electrode chopped  $J$ - $V$  curve of sample B in 0.5 M  $\text{H}_2\text{SO}_4$  under dark and AM 1.5G one illumination. The photocathode sample area is 0.025  $\text{cm}^2$ .

Figure 3d shows Pt nanoparticle coverage on the sidewall of the nanowire and on the top/bottom surfaces as the images show a 3D projection of the structure onto a 2D image. The EELS elemental mappings in Figure 3d clearly show the presence of Al (red) and Pt (green) on the sidewall of the nanowire. The thickness of the  $\text{Al}_2\text{O}_3$  layer on the nanowire from Figure 3d is found to be  $\sim 1$ – $2$  nm, which is in good agreement with the thickness calibration by ALD. In addition, the energy-dispersive X-ray spectroscopy (EDX) mapping, as indicated by A and B regions in Figure S4a,b, further shows the presence of  $\text{Al}_2\text{O}_3$  on the nanowires. These results confirm the conformal coverage of  $\text{Al}_2\text{O}_3$  over the nanowires and Pt nanoparticles.

Listed in Table T2, three different samples were studied to elucidate the PEC properties of the InGaN/Si double-junction photocathode. Sample A,  $n^+$ -InGaN/Si, is a platinized single-junction photocathode without the tunnel junction or the top  $p^+$ -InGaN segment, which serves as a control sample. It has similar working principle as the previously reported GaN/Si single-junction photocathodes.<sup>25,37,55</sup> Samples B and C are the platinized double-junction samples with and without  $\text{Al}_2\text{O}_3$  passivation layer, respectively. The PEC performance comparisons between these three samples clearly show the effects of the tunnel junction, the top  $p^+$ -InGaN subcell, and the  $\text{Al}_2\text{O}_3$  passivation layer in reducing kinetic losses, enhancing open-circuit potential, and improving device stability, respectively. The PEC experimental conditions are described in Supporting Information Section S1. Figure 4a shows the three-electrode linear scan voltammogram (LSV) comparison between sample B (red curve) and sample A (blue curve) under AM 1.5G one sun illumination and dark conditions (green curve). Sample A (single-junction Si) has  $V_{\text{on}}$  of  $\sim 0.5$  V vs RHE, whereas sample B (double-junction InGaN/TJ/Si) has  $V_{\text{on}}$  of  $\sim 2.3$  V vs RHE. Compared to Figure 1b, the  $V_{\text{on}}$  of sample B is  $\sim 100$  mV higher than that of the theoretically calculated ideal  $\text{In}_{0.46}\text{Ga}_{0.54}\text{N/Si}$  double junction and  $\sim 300$  mV lower than the theoretically calculated ideal  $\text{In}_{0.32}\text{Ga}_{0.68}\text{N/Si}$  double junction. As shown in Figure 1b, the  $V_{\text{on}}$  difference of  $\sim 400$  mV between ideal  $\text{In}_{0.46}\text{Ga}_{0.54}\text{N/Si}$  and  $\text{In}_{0.32}\text{Ga}_{0.68}\text{N/Si}$  double-junction devices is directly correlated to the difference between the band gap of the top junctions. However, the variations in the  $V_{\text{on}}$  and fill factors between the theoretical simulations (Figure 1b) and experimental results (Figure 4a) are because in the simulation we have assumed ideal ohmic contacts, without any voltage loss, for tunnel junction interface, back side metal contacts, and

semiconductor/liquid interface (see Table T1). Shown in Figure S5, the open-circuit potential (OCP) measurements versus RHE under chopped light illumination for sample B exhibit a dark potential  $\sim 0.3$  V and light potential  $\sim 2.3$  V (same as  $V_{\text{on}}$ ), with a change in OCP of  $\sim 2$  V. Assuming a relatively small HER overpotential,<sup>56</sup> the  $V_{\text{on}}$  will be close to flat-band potential ( $V_{\text{fb}}$ ) derived from the Mott–Schottky measurements (see Figure S6). As shown in Figure 4a, the maximum saturation photocurrent density for sample B is  $\sim 9$   $\text{mA}/\text{cm}^2$  at 0.3 V vs RHE. Compared to sample A, the photocurrent density for sample B is lower at 0.3 V vs RHE. This is because the device is limited by the top  $p^+$ -InGaN segment (with a band gap of  $\sim 2.2$  eV), which can give a theoretical maximum of up to 10  $\text{mA}/\text{cm}^2$ ,<sup>57</sup> whereas the single-junction photocathode (sample A, Si being the primary light absorber) has a theoretical maximum photocurrent density of  $\sim 44$   $\text{mA}/\text{cm}^2$ .<sup>57</sup> Due to indium compositional variations, the theoretical current density for the top cell could also be higher than that mentioned above. Further details of the three-electrode  $J$ - $V$  measurements are explained in Figure S7a. The applied bias photon-to-current efficiency (ABPE) of this photocathode is  $\sim 9.6\%$  at 1.3 V vs RHE (see Figure S7b). The reported ABPE is one of the highest for Si-based photocathodes.<sup>46,58–60</sup>

Figure 4b shows the chopped two-electrode LSV of sample B under AM 1.5G one sun illumination and dark conditions. The PEC performance optimization of the photocathode in terms of  $\text{Al}_2\text{O}_3$  deposition conditions is discussed in Figure S8a,b. The OCP (see Figure S5) and Mott–Schottky (see Figure S6) measurements clearly show that sample B can perform unassisted water splitting with sufficient photovoltage to overcome the water redox potentials including the HER overpotential.<sup>3</sup> As shown in Figure 4b, the maximum photocurrent density for sample B, at 0 V vs  $\text{IrO}_x$ , is  $\sim 8.4$   $\text{mA}/\text{cm}^2$  with  $V_{\text{on}}$  of  $\sim 0.7$  V vs  $\text{IrO}_x$  under AM 1.5G one sun illumination in 0.5 M  $\text{H}_2\text{SO}_4$ . It is worth mentioning that the significant indium compositional variations in the nanowires may also impact  $V_{\text{on}}$ . In Figure S8c, the photocurrent density of sample B, with optimized  $\text{Al}_2\text{O}_3$  thin film, is higher than that of sample C ( $\sim 5.5$   $\text{mA}/\text{cm}^2$ ) at 0 V vs  $\text{IrO}_x$ . It is clear from the light LSV curve (blue curve) in Figure S8c, for sample C, that there is considerable surface recombination within the structure, which gives a poor fill factor and thereby reduces the saturated photocurrent density of this device. As shown in Figure S9, the PL intensity of the InGaN/Si sample (black curve) is reduced after depositing



**Figure 5.** Impedance spectroscopy of surface-modified InGaN/Si double-junction photocathode. (a) Nyquist plots of sample B (red curve) and sample A (blue curve) in 0.5 M  $\text{H}_2\text{SO}_4$  at 1.2 V vs RHE under AM 1.5G one sun illumination. (b) Nyquist plots of sample B (red curve) and sample C (black curve) in 0.5 M  $\text{H}_2\text{SO}_4$  at 0 V vs  $\text{IrO}_x$  under AM 1.5G one sun illumination.

Pt nanoparticles, which can be explained by the enhanced charge carrier separation and extraction due to the formation of the Schottky barrier<sup>61</sup> at the interface of InGaN and Pt. In contrast, the PL intensity of the platinized InGaN/Si sample after deposition of a thin  $\text{Al}_2\text{O}_3$  layer (blue curve) is increased because of the reduction in surface recombination. The effect of  $\text{Al}_2\text{O}_3$  on the double junction in terms of improving charge-transfer characteristics is further discussed below. The STH (at 0 V vs  $\text{IrO}_x$ ), calculated using eq 3 in the Supporting Information (see Section S1), for sample B is 10.3% under AM 1.5G one sun illumination. As shown in Figure 1a, to the best of our knowledge, this is the highest STH for Si and non-III–V-based photocathodes.<sup>16,18,19,62,63</sup> From theoretical simulations (see Figure 1b), the photocurrent density and STH of an ideal InGaN/Si double-junction photocathode, with energy band gaps of  $\sim 2.2$  and 1.1 eV, is  $\sim 10 \text{ mA/cm}^2$  and 12.3%, respectively, which can be further improved by optimizing the energy band gap of InGaN. Experimentally, the broad indium compositional variations in nanowire structures, i.e., a significant portion of the nanowires or nanowire regions showing energy band gap less than 2.2 eV, may also lead to enhanced light absorption (and therefore higher photocurrent) compared to a single band gap material. There is significant room for improving the light absorption and charge-transfer kinetics of InGaN/Si photocathode (discussed in Supporting Information Section S2) and surface passivation to achieve higher STH. Apart from the two-electrode LSV measurements, it is essential to study the spectral response of the double-junction photocathode. A tandem photoelectrode requires customized incident photon-to-current conversion efficiency (IPCE) analysis to each subcell, as per the protocols,<sup>57</sup> to determine the maximum STH under the two-electrode configuration.<sup>57,62,64</sup> It is to be noted that IPCE measurement of a tandem photoelectrode is significantly more challenging and complex when compared to single-junction devices because of the two-terminal configuration wherein the subcells cannot be individually measured. The critical challenges of performing IPCE measurements for a two-terminal tandem device, such as InGaN/Si photocathode, include (1) light bias must be carefully filtered<sup>65</sup> and intensity tuned to obtain specific spectral responses and reduced nonradiative recombination,<sup>66</sup> respectively, for two junctions and (2) the subcell being investigated must be current-limiting over the entire spectral range.<sup>7</sup> Furthermore, the low-intensity monochromatic irradiation leads to a small photocurrent, and

any discrepancy in photocathode active-area calculation will significantly under or overestimate IPCE results.<sup>67</sup> Hence, to avoid errors in surface area calculations, it is necessary to perform area-independent IPCE measurements<sup>9,67</sup> by covering the photocathode surface area with an inert mask having a well-defined opening to expose certain sample region and shield the rest of the sample area. In future studies, appropriate IPCE experimental protocols will be utilized to gain further insights in the spectral response of the InGaN/Si double-junction photocathode.

Further detailed electrochemical impedance spectroscopy (EIS) measurements were performed in 0.5 M  $\text{H}_2\text{SO}_4$  under AM 1.5G one sun illumination for both two- and three-electrode configurations (see Supporting Information Section S1) for different samples to understand the charge-transfer characteristics. Figure 5a shows the Nyquist plots between sample A (blue) and sample B (red). The  $R_{ct}$  is calculated using the equivalent circuit models derived from these plots.<sup>25</sup> It is noted that sample B has the lowest  $R_{ct}$  ( $< 150 \Omega \text{ cm}^2$ ) at an applied bias 1.2 V vs RHE compared to sample A ( $> 10\,000 \Omega \text{ cm}^2$ ). This result shows that the top  $p^+$ -InGaN under illumination gives out photogenerated electrons, which are efficiently transferred to the electrolyte through the surface modification layers (i.e., Pt nanoparticles and  $\text{Al}_2\text{O}_3$ ), and the photogenerated holes recombine with the electrons from the bottom Si without any significant losses in the TJ.

As discussed previously, the  $\text{Al}_2\text{O}_3$  passivation layer helps in improving the LSV characteristics for the double-junction device (see Figure S8c). Figure 5b shows the two-electrode EIS measurements at 0 V vs  $\text{IrO}_x$  for samples B and C. The semicircle arc in the lower-frequency range for the double-junction photocathode with  $\text{Al}_2\text{O}_3$  has a smaller diameter compared to the one without  $\text{Al}_2\text{O}_3$ , which is due to the reduction in charge carrier recombination (see Figure S9), especially in the  $p^+$ -InGaN segment. Because the nanowires are coated with relatively thin ALD  $\text{Al}_2\text{O}_3$  films, the photogenerated electrons can easily tunnel through the passivation layer and participate in HER. Thus, the  $\text{Al}_2\text{O}_3$  thin-film further helps in reducing HER overpotential which has been previously observed in Si-based photocathodes.<sup>45,46</sup> This  $\text{Al}_2\text{O}_3$  film also acts as a protection layer<sup>45–47</sup> for the nanowires and assists in improving the stability of the double-junction photocathode. To the best of our knowledge, this is the first demonstration of a thin passivation



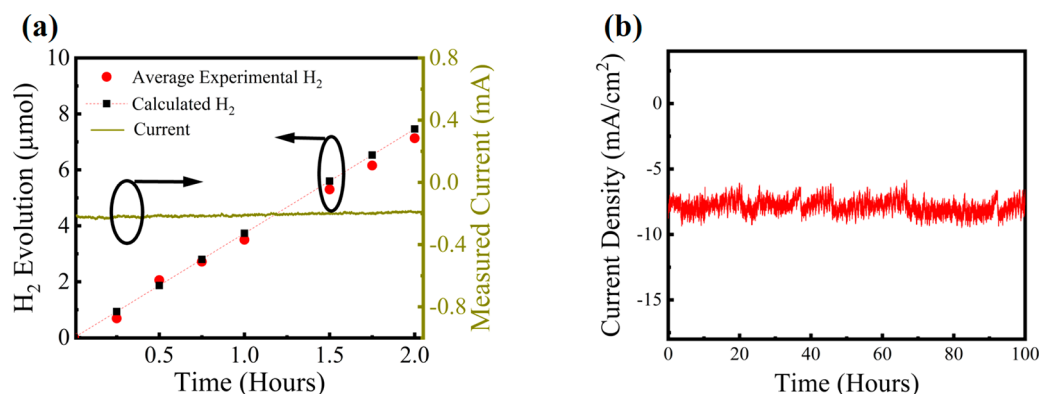


**Figure 6.** Hydrogen evolution and stability measurements of surface-modified InGaN/Si double-junction photocathode. (a) H<sub>2</sub> generation for sample B at 0 V vs IrO<sub>x</sub> under AM 1.5G one sun illumination in 0.5 M H<sub>2</sub>SO<sub>4</sub> for 2 h. (b) Long-term stability measurement for sample B at 0 V vs IrO<sub>x</sub> in 0.5 M H<sub>2</sub>SO<sub>4</sub> under AM 1.5G one sun illumination.

layer being deposited on the cocatalyst-modified light absorber to enhance charge transfer and reduce surface recombination.

We have evaluated the Faraday efficiency (see Supporting Information Section S1) by analyzing the H<sub>2</sub> generation from sample B. Shown in Figure 6a, the photocurrent and H<sub>2</sub> evolution are simultaneously measured at 0 V vs IrO<sub>x</sub> for a duration of 2 h in 0.5 M H<sub>2</sub>SO<sub>4</sub> under AM 1.5G one sun illumination. The Faraday efficiency ( $\eta_{\text{Faraday}}$ ) is calculated using eq 5 in the Supporting Information (see Section S1), and it is in the range of 95–100%. We further conducted a long duration stability test for sample B at 0 V vs IrO<sub>x</sub> in 0.5 M H<sub>2</sub>SO<sub>4</sub> with 1 mM Triton X-100 surfactant under AM 1.5G one sun illumination. As shown in Figure 6b, the photocurrent density showed no degradation for a duration of 100 h. To maintain the same experimental conditions throughout the stability test, the electrolyte was changed after every 24 h. The current density varied within 10–20% of the average photocurrent density  $\sim 8.2$  mA/cm<sup>2</sup>, which corresponds to STH variation of  $\sim 9 \pm 1.5\%$  throughout the stability experiments. The observed fluctuations in photocurrent are due to the changes in the potential of the counter electrode at 0 V vs IrO<sub>x</sub>. This high stability at STH  $\approx 10\%$ , as shown in Figure 1a, is the longest stability reported for any photoelectrodes including III–V photoelectrodes in two-electrode configurations.<sup>9–13,16,18,20,62,68</sup>

The structural analysis after 100 h experiments is confirmed by SEM studies. The SEM image in Figure S10 shows that nanowires have no changes in dimensions (length,  $\sim 600$ – $700$  nm; diameter,  $\sim 80$  nm) and coverage over the Si surface compared to those taken before stability testing, shown in Figures 2a and S2. X-ray diffraction measurements (see Figure S11) show nearly identical peak positions at  $\sim 34.5^\circ$  for the samples before and after the stability test. Moreover, XPS measurements after the stability test, shown in Figure S12, reveal Pt 4f and Al 2p peaks at  $70.5^\circ$  and  $74.1^\circ$ , respectively. The above measurements confirm the presence of an Al<sub>2</sub>O<sub>3</sub> protection layer and Pt nanoparticles on InGaN nanowires after the long-term stability test.

To date, the major challenges for unassisted photoelectrochemical water splitting include (i) design and synthesis of tandem photoelectrodes,<sup>7,69</sup> (ii) STH efficiency and stability of the photoelectrodes,<sup>8,70</sup> and (iii) manufacturing cost and scalability<sup>2,6</sup> of the photoelectrodes. As discussed earlier, III–V compound semiconductor multijunction photoelectrodes (see Figure 1a) can achieve high efficiency, but they are plagued by poor stability and high material synthesis cost.<sup>9,11,12</sup> The reasons

for the instability of III–V photoelectrodes in electrolytes (see Figure 1a) include photocorrosion of the light absorber,<sup>10,11,62</sup> pinholes in passivation layers,<sup>11</sup> and insufficient cocatalyst coverage over the light absorber.<sup>71</sup> It is evident that the Al<sub>2</sub>O<sub>3</sub>/Pt/*p*<sup>+</sup>-InGaN/TJ/*n*<sup>+</sup>-*p* Si double-junction photocathode can sustain high STH value of  $>10\%$  and stability of 100 h, because of the N-terminated nanowires which have nearly perfect single-wurtzite structure with negligible defects or dislocations.<sup>35</sup> Because of the unique polarization-induced TJ incorporated in the nanowires,<sup>72–74</sup> the charge carriers from the top *p*<sup>+</sup>-InGaN cell (photogenerated holes) can readily tunnel and recombine with charge carriers (photogenerated electrons) from bottom Si subcell in the TJ (see Figures 1c, 2c, and 3c). One of the critical limitations for this structural design, however, is the surface recombination at the top *p*<sup>+</sup>-InGaN segment. As shown in Figures 5b and S8c, there are some surface recombination sites at the Pt/*p*<sup>+</sup>-InGaN interface which give rise to a lower *J*, poor fill factor, higher *R<sub>s</sub>* values, and sensitivity to device fabrication/synthesis conditions. Depositing a thin Al<sub>2</sub>O<sub>3</sub> layer on the nanowire surface helps in reducing the surface recombination (see Figure S9), which acts as an efficient tunneling layer for electrons from Pt/*p*<sup>+</sup>-InGaN to the electrolyte and further protects the nanowire against corrosion. Because of the efficient InGaN/Si photocathode design and Al<sub>2</sub>O<sub>3</sub> protection layer, the device is capable of performing unassisted water splitting.<sup>24</sup> Further optimization in the design and epitaxy of In-rich InGaN (with band gap of  $\sim 1.8$  eV) will provide a path to achieve STH  $> 15\%$ .

The high stability for Al<sub>2</sub>O<sub>3</sub>/Pt/*p*<sup>+</sup>-InGaN/TJ nanowires/*n*<sup>+</sup>-*p* Si photocathode is also attributed to the stability of III-nitride nanowires. It is known that III-nitrides have strong ionic bonds compared to other III–V semiconductors, with surface states bunched near the band edges, which make them resistant against corrosion in different electrolytes.<sup>35,75,76</sup> Recent studies show that MBE-grown III-nitrides have unique N-termination not only on their top *c*-plane but also along the nonpolar sidewalls.<sup>35</sup> Such N-terminated nanowires experimentally demonstrated high stability of  $>500$  h under photocatalytic water-splitting conditions with no additional protection layers<sup>34</sup> and  $>3000$  h under PEC water-splitting conditions under three-electrode measurements.<sup>37</sup> Previous studies show that N-terminated InGaN nanowires on nonplanar Si wafers, without any additional protection layer, can achieve high stability  $\sim 30$  h with high *J*  $\approx 12$  mA/cm<sup>2</sup> at 0 V vs RHE in 0.5 M H<sub>2</sub>SO<sub>4</sub> under AM 1.5G one sun illumination.<sup>42</sup> Therefore, *p*<sup>+</sup>-InGaN

nanowires are stable in acidic solution and can protect the underlying Si wafer against photocorrosion, which makes this double-junction photocathode a viable option for large-scale implementation of high-efficiency PEC water splitting.

In conclusion, we have demonstrated a new class of InGaN/Si-based double-junction photoelectrodes, which can achieve relatively efficient, stable, unassisted PEC water splitting. The MBE-grown InGaN TJ nanowires on Si have high-crystalline quality, large surface area, and N-termination on both polar and nonpolar side faces, which protects against photocorrosion for the entire structure without compromising the PEC performance. Impedance studies further showed the importance of top  $p^+$ -InGaN segment, tunnel junction and surface modifications in improving electron extraction and reducing surface recombination. The  $\text{Al}_2\text{O}_3/\text{Pt}/p^+\text{-InGaN}/\text{TJ}/n^+\text{-p Si}$  photocathode exhibits a maximum photocurrent density of  $\sim 8.4 \text{ mA/cm}^2$  at 0 V vs  $\text{IrO}_x$  under AM 1.5G one sun illumination in 0.5 M  $\text{H}_2\text{SO}_4$ . Our studies provide a platform for developing industry-ready materials to achieve highly efficient and stable unassisted solar water splitting for low-cost  $\text{H}_2$  production.

## ■ ASSOCIATED CONTENT

### ■ Supporting Information

The Supporting Information is available free of charge at <https://pubs.acs.org/doi/10.1021/acsenerylett.0c01583>.

Methods section, indium variation across the sample area; table showing the summary of main parameters used for simulation of an ideal  $\text{In}_{0.46}\text{Ga}_{0.54}\text{N}/\text{Si}$  tandem device; table showing the summary of single- and double-junction photocathodes used in the PEC experiments; SEM image of InGaN/Si photocathode after surface modifications; STEM image and EDS mapping of different regions of InGaN nanowires; OCP measurements in three-electrode configuration; Mott–Schottky measurements in three-electrode configuration; LSV and ABPE measurements in three-electrode configuration; PL comparison between as-grown InGaN/Si, InGaN/Si with Pt, and InGaN/Si with  $\text{Pt}/\text{Al}_2\text{O}_3$ ; photocathode optimization by varying ALD  $\text{Al}_2\text{O}_3$  deposition conditions; SEM image after stability experiment; XPS measurements after stability test XRD results before and after stability test (PDF)

## ■ AUTHOR INFORMATION

### Corresponding Author

**Zetian Mi** – Department of Electrical Engineering and Computer Science, University of Michigan, Ann Arbor, Ann Arbor, Michigan 48109, United States; [orcid.org/0000-0001-9494-7390](https://orcid.org/0000-0001-9494-7390); Phone: 1 734 764 3963; Email: [ztmi@umich.edu](mailto:ztmi@umich.edu)

### Authors

**Srinivas Vanka** – Department of Electrical Engineering and Computer Science, University of Michigan, Ann Arbor, Ann Arbor, Michigan 48109, United States; [orcid.org/0000-0001-8474-2244](https://orcid.org/0000-0001-8474-2244)

**Baowen Zhou** – Department of Electrical Engineering and Computer Science, University of Michigan, Ann Arbor, Ann Arbor, Michigan 48109, United States; [orcid.org/0000-0003-2476-0322](https://orcid.org/0000-0003-2476-0322)

**Rasha A. Awani** – Department of Physics and Astronomy, and Wright Center for Photovoltaics Innovation and

Commercialization (PVIC), University of Toledo, Toledo, Ohio 43606, United States

**Zhaoning Song** – Department of Physics and Astronomy, and Wright Center for Photovoltaics Innovation and Commercialization (PVIC), University of Toledo, Toledo, Ohio 43606, United States; [orcid.org/0000-0002-6677-0994](https://orcid.org/0000-0002-6677-0994)

**Faqrul A. Chowdhury** – Department of Physics, McGill University, Montreal, Québec H3A 2T8, Canada; Department of Engineering Physics, Polytechnique Montreal, Montreal, Quebec H3T 1J4, Canada; [orcid.org/0000-0001-9747-5368](https://orcid.org/0000-0001-9747-5368)

**Xuedong Liu** – Facility for Electron Microscopy Research, McGill University, Montreal, Quebec H3A 0C7, Canada

**Hamed Hajibabaei** – Department of Chemistry, Michigan State University, East Lansing, Michigan 48824-1322, United States

**Wen Shi** – Department of Materials Science and Engineering, McMaster University, Hamilton, Ontario L8S 4M1, Canada

**Yixin Xiao** – Department of Electrical Engineering and Computer Science, University of Michigan, Ann Arbor, Ann Arbor, Michigan 48109, United States

**Ishtiaque A. Navid** – Department of Electrical Engineering and Computer Science, University of Michigan, Ann Arbor, Ann Arbor, Michigan 48109, United States

**Ayush Pandey** – Department of Electrical Engineering and Computer Science, University of Michigan, Ann Arbor, Ann Arbor, Michigan 48109, United States

**Rong Chen** – Department of Chemistry, Boston College, Chestnut Hill, Massachusetts 02467, United States

**Gianluigi A. Botton** – Department of Materials Science and Engineering, McMaster University, Hamilton, Ontario L8S 4M1, Canada; [orcid.org/0000-0002-8746-1146](https://orcid.org/0000-0002-8746-1146)

**Thomas W. Hamann** – Department of Chemistry, Michigan State University, East Lansing, Michigan 48824-1322, United States; [orcid.org/0000-0001-6917-7494](https://orcid.org/0000-0001-6917-7494)

**Dunwei Wang** – Department of Chemistry, Boston College, Chestnut Hill, Massachusetts 02467, United States; [orcid.org/0000-0001-5581-8799](https://orcid.org/0000-0001-5581-8799)

**Yanfa Yan** – Department of Physics and Astronomy, and Wright Center for Photovoltaics Innovation and Commercialization (PVIC), University of Toledo, Toledo, Ohio 43606, United States; [orcid.org/0000-0003-3977-5789](https://orcid.org/0000-0003-3977-5789)

Complete contact information is available at: <https://pubs.acs.org/doi/10.1021/acsenerylett.0c01583>

### Notes

The authors declare the following competing financial interest(s): Some IP related to the synthesis of InGaN nanowires was licensed to NS Nanotech, which was co-founded by Z. Mi.

## ■ ACKNOWLEDGMENTS

The authors gratefully acknowledge research support from the HydroGEN Advanced Water Splitting Materials Consortium, established as part of the Energy Materials Network under the U.S. Department of Energy, Office of Energy Efficiency and Renewable Energy, Fuel Cell Technologies Office, under Award Number DE-EE0008086. The electron energy spectroscopy work was carried out at the Canadian Centre for Electron Microscopy, a national facility supported by the Canada Foundation for Innovation under the Major Science Initiatives,



the Natural Sciences and Engineering Research Council, and McMaster University.

## REFERENCES

- (1) Tuller, H. L. Solar to fuels conversion technologies: a perspective. *Mater. Renew. Sustain. Energy* **2017**, *6* (1), 3.
- (2) Shaner, M. R.; Atwater, H. A.; Lewis, N. S.; McFarland, E. W. A comparative technoeconomic analysis of renewable hydrogen production using solar energy. *Energy Environ. Sci.* **2016**, *9* (7), 2354–2371.
- (3) Chu, S.; Li, W.; Yan, Y.; Hamann, T.; Shih, I.; Wang, D.; Mi, Z. Roadmap on solar water splitting: current status and future prospects. *Nano Futures* **2017**, *1* (2), 022001.
- (4) Lopes, T.; Dias, P.; Andrade, L.; Mendes, A. An innovative photoelectrochemical lab device for solar water splitting. *Sol. Energy Mater. Sol. Cells* **2014**, *128*, 399–410.
- (5) Lewis, N. S. Research opportunities to advance solar energy utilization. *Science* **2016**, *351* (6271), aad1920.
- (6) Pinaud, B. A.; Benck, J. D.; Seitz, L. C.; Forman, A. J.; Chen, Z.; Deutsch, T. G.; James, B. D.; Baum, K. N.; Baum, G. N.; Ardo, S.; Wang, H.; Miller, E.; Jaramillo, T. F. Technical and economic feasibility of centralized facilities for solar hydrogen production via photocatalysis and photoelectrochemistry. *Energy Environ. Sci.* **2013**, *6* (7), 1983.
- (7) Prévot, M. S.; Sivula, K. Photoelectrochemical Tandem Cells for Solar Water Splitting. *J. Phys. Chem. C* **2013**, *117* (35), 17879–17893.
- (8) Fountaine, K. T.; Lewerenz, H. J.; Atwater, H. A. Efficiency limits for photoelectrochemical water-splitting. *Nat. Commun.* **2016**, *7*, 13706.
- (9) Young, J. L.; Steiner, M. A.; Döschner, H.; France, R. M.; Turner, J. A.; Deutsch, T. G. Direct solar-to-hydrogen conversion via inverted metamorphic multi-junction semiconductor architectures. *Nat. Energy* **2017**, *2*, 17028.
- (10) Khaselev, O.; Turner, J. A. A monolithic photovoltaic-photoelectrochemical device for hydrogen production via water splitting. *Science* **1998**, *280* (5362), 425–427.
- (11) Verlage, E.; Hu, S.; Liu, R.; Jones, R. J. R.; Sun, K.; Xiang, C.; Lewis, N. S.; Atwater, H. A. A monolithically integrated, intrinsically safe, 10% efficient, solar-driven water-splitting system based on active, stable earth-abundant electrocatalysts in conjunction with tandem III–V light absorbers protected by amorphous TiO<sub>2</sub> films. *Energy Environ. Sci.* **2015**, *8* (11), 3166–3172.
- (12) Cheng, W.-H.; Richter, M. H.; May, M. M.; Ohlmann, J.; Lackner, D.; Dimroth, F.; Hannappel, T.; Atwater, H. A.; Lewerenz, H.-J. Monolithic Photoelectrochemical Device for Direct Water Splitting with 19% Efficiency. *ACS Energy Lett.* **2018**, *3* (8), 1795–1800.
- (13) Kang, D.; Young, J. L.; Lim, H.; Klein, W. E.; Chen, H.; Xi, Y.; Gai, B.; Deutsch, T. G.; Yoon, J. Printed assemblies of GaAs photoelectrodes with decoupled optical and reactive interfaces for unassisted solar water splitting. *Nat. Energy* **2017**, *2*, 17043.
- (14) Ostermayer, F. W.; Kohl, P. A. Photoelectrochemical etching of p-GaAs. *Appl. Phys. Lett.* **1981**, *39* (1), 76–78.
- (15) Nandjou, F.; Haussener, S. Degradation in photoelectrochemical devices: review with an illustrative case study. *J. Phys. D: Appl. Phys.* **2017**, *50* (12), 124002.
- (16) Reece, S. Y.; Hamel, J. A.; Sung, K.; Jarvi, T. D.; Esswein, A. J.; Pijpers, J. J. H.; Nocera, D. G. Wireless Solar Water Splitting Using Silicon-Based Semiconductors and Earth-Abundant Catalysts. *Science* **2011**, *334* (6056), 645–648.
- (17) Abdi, F. F.; Han, L.; Smets, A. H.; Zeman, M.; Dam, B.; van de Krol, R. Efficient solar water splitting by enhanced charge separation in a bismuth vanadate-silicon tandem photoelectrode. *Nat. Commun.* **2013**, *4*, 2195.
- (18) Kim, J. H.; Jo, Y.; Kim, J. H.; Jang, J. W.; Kang, H. J.; Lee, Y. H.; Kim, D. S.; Jun, Y.; Lee, J. S. Wireless Solar Water Splitting Device with Robust Cobalt-Catalyzed, Dual-Doped BiVO<sub>4</sub> Photoanode and Perovskite Solar Cell in Tandem: A Dual Absorber Artificial Leaf. *ACS Nano* **2015**, *9* (12), 11820–11829.
- (19) Shi, X.; Zhang, K.; Shin, K.; Ma, M.; Kwon, J.; Choi, I. T.; Kim, J. K.; Kim, H. K.; Wang, D. H.; Park, J. H. Unassisted photoelectrochemical water splitting beyond 5.7% solar-to-hydrogen conversion efficiency by a wireless monolithic photoanode/dye-sensitized solar cell tandem device. *Nano Energy* **2015**, *13*, 182–191.
- (20) Kim, J. H.; Jang, J. W.; Jo, Y. H.; Abdi, F. F.; Lee, Y. H.; van de Krol, R.; Lee, J. S. Hetero-type dual photoanodes for unbiased solar water splitting with extended light harvesting. *Nat. Commun.* **2016**, *7*, 13380.
- (21) Steier, L.; Herraiz-Cardona, I.; Gimenez, S.; Fabregat-Santiago, F.; Bisquert, J.; Tilley, S. D.; Grätzel, M. Understanding the Role of Underlayers and Overlayers in Thin Film Hematite Photoanodes. *Adv. Funct. Mater.* **2014**, *24* (48), 7681–7688.
- (22) Dias, P.; Vilanova, A.; Lopes, T.; Andrade, L.; Mendes, A. Extremely stable bare hematite photoanode for solar water splitting. *Nano Energy* **2016**, *23*, 70–79.
- (23) Bae, D.; Seger, B.; Vesborg, P. C.; Hansen, O.; Chorkendorff, I. Strategies for stable water splitting via protected photoelectrodes. *Chem. Soc. Rev.* **2017**, *46* (7), 1933–1954.
- (24) Kibria, M. G.; Chowdhury, F. A.; Zhao, S.; AlOtaibi, B.; Trudeau, M. L.; Guo, H.; Mi, Z. Visible light-driven efficient overall water splitting using p-type metal-nitride nanowire arrays. *Nat. Commun.* **2015**, *6*, 6797.
- (25) Vanka, S.; Arca, E.; Cheng, S.; Sun, K.; Botton, G. A.; Teeter, G.; Mi, Z. High Efficiency Si Photocathode Protected by Multifunctional GaN Nanostructures. *Nano Lett.* **2018**, *18* (10), 6530–6537.
- (26) AlOtaibi, B.; Nguyen, H. P.; Zhao, S.; Kibria, M. G.; Fan, S.; Mi, Z. Highly stable photoelectrochemical water splitting and hydrogen generation using a double-band InGaN/GaN core/shell nanowire photoanode. *Nano Lett.* **2013**, *13* (9), 4356–4361.
- (27) AlOtaibi, B.; Harati, M.; Fan, S.; Zhao, S.; Nguyen, H. P.; Kibria, M. G.; Mi, Z. High efficiency photoelectrochemical water splitting and hydrogen generation using GaN nanowire photoelectrode. *Nanotechnology* **2013**, *24* (17), 175401.
- (28) Varadhan, P.; Fu, H. C.; Priante, D.; Retamal, J. R.; Zhao, C.; Ebaid, M.; Ng, T. K.; Ajia, I.; Mitra, S.; Roqan, I. S.; Ooi, B. S.; He, J. H. Surface Passivation of GaN Nanowires for Enhanced Photoelectrochemical Water-Splitting. *Nano Lett.* **2017**, *17* (3), 1520–1528.
- (29) ElAfandy, R. T.; Ebaid, M.; Min, J. W.; Zhao, C.; Ng, T. K.; Ooi, B. S. Flexible InGaN nanowire membranes for enhanced solar water splitting. *Opt. Express* **2018**, *26* (14), A640–A650.
- (30) Kibria, M. G.; Mi, Z. Artificial photosynthesis using metal/nonmetal-nitride semiconductors: current status, prospects, and challenges. *J. Mater. Chem. A* **2016**, *4* (8), 2801–2820.
- (31) Luo, W.; Liu, B.; Li, Z.; Xie, Z.; Chen, D.; Zou, Z.; Zhang, R. Stable response to visible light of InGaN photoelectrodes. *Appl. Phys. Lett.* **2008**, *92* (26), 262110.
- (32) Kibria, M. G.; Nguyen, H. P. T.; Cui, K.; Zhao, S.; Liu, D.; Guo, H.; Trudeau, M. L.; Paradis, S.; Hakima, A.-R.; Mi, Z. One-Step Overall Water Splitting under Visible Light Using Multiband InGaN/GaN Nanowire Heterostructures. *ACS Nano* **2013**, *7* (9), 7886–7893.
- (33) Chowdhury, F. A.; Trudeau, M. L.; Guo, H.; Mi, Z. A photochemical diode artificial photosynthesis system for unassisted high efficiency overall pure water splitting. *Nat. Commun.* **2018**, *9* (1), 1707.
- (34) Guan, X.; Chowdhury, F. A.; Wang, Y.; Pant, N.; Vanka, S.; Trudeau, M. L.; Guo, L.; Vayssieres, L.; Mi, Z. Making of an Industry-Friendly Artificial Photosynthesis Device. *ACS Energy Lett.* **2018**, *3* (9), 2230–2231.
- (35) Kibria, M. G.; Qiao, R.; Yang, W.; Boukahil, I.; Kong, X.; Chowdhury, F. A.; Trudeau, M. L.; Ji, W.; Guo, H.; Himpel, F. J.; Vayssieres, L.; Mi, Z. Atomic-Scale Origin of Long-Term Stability and High Performance of p-GaN Nanowire Arrays for Photocatalytic Overall Pure Water Splitting. *Adv. Mater.* **2016**, *28* (38), 8388–8397.
- (36) Su, J.; Wei, Y.; Vayssieres, L. Stability and Performance of Sulfide-, Nitride-, and Phosphide-Based Electrodes for Photocatalytic Solar Water Splitting. *J. Phys. Chem. Lett.* **2017**, *8* (20), 5228–5238.
- (37) Vanka, S.; Sun, K.; Zeng, G.; Pham, T. A.; Toma, F. M.; Ogitsu, T.; Mi, Z. Long-term stability studies of a semiconductor photoelectrode in three-electrode configuration. *J. Mater. Chem. A* **2019**, *7*, 27612–27619.

- (38) Fan, R.; Dong, W.; Fang, L.; Zheng, F.; Shen, M. More than 10% efficiency and one-week stability of Si photocathodes for water splitting by manipulating the loading of the Pt catalyst and TiO<sub>2</sub> protective layer. *J. Mater. Chem. A* **2017**, *5*, 18744–18751.
- (39) Chowdhury, F. A.; Mi, Z.; Kibria, M. G.; Trudeau, M. L. Group III-nitride nanowire structures for photocatalytic hydrogen evolution under visible light irradiation. *APL Mater.* **2015**, *3* (10), 104408.
- (40) Moses, P. G.; Miao, M.; Yan, Q.; Van de Walle, C. G. Hybrid functional investigations of band gaps and band alignments for AlN, GaN, InN, and InGaN. *J. Chem. Phys.* **2011**, *134* (8), 084703.
- (41) Sadaf, S. M.; Ra, Y. H.; Szkopek, T.; Mi, Z. Monolithically Integrated Metal/Semiconductor Tunnel Junction Nanowire Light-Emitting Diodes. *Nano Lett.* **2016**, *16* (2), 1076–80.
- (42) Wang, Y.; Vanka, S.; Gim, J.; Wu, Y.; Fan, R.; Zhang, Y.; Shi, J.; Shen, M.; Hovden, R.; Mi, Z. An In<sub>0.42</sub>Ga<sub>0.58</sub>N tunnel junction nanowire photocathode monolithically integrated on a nonplanar Si wafer. *Nano Energy* **2019**, *57*, 405–413.
- (43) Fan, S.; Alotaibi, B.; Woo, S. Y.; Wang, Y.; Botton, G. A.; Mi, Z. High efficiency solar-to-hydrogen conversion on a monolithically integrated InGa<sub>N</sub>/Ga<sub>N</sub>/Si adaptive tunnel junction photocathode. *Nano Lett.* **2015**, *15* (4), 2721–6.
- (44) Ros, C.; Andreu, T.; Morante, J. R. Photoelectrochemical water splitting: a road from stable metal oxides to protected thin film solar cells. *J. Mater. Chem. A* **2020**, *8* (21), 10625–10669.
- (45) Choi, M. J.; Jung, J.-Y.; Park, M.-J.; Song, J.-W.; Lee, J.-H.; Bang, J. H. Long-term durable silicon photocathode protected by a thin Al<sub>2</sub>O<sub>3</sub>/SiO<sub>x</sub> layer for photoelectrochemical hydrogen evolution. *J. Mater. Chem. A* **2014**, *2* (9), 2928.
- (46) Fan, R.; Dong, W.; Fang, L.; Zheng, F.; Su, X.; Zou, S.; Huang, J.; Wang, X.; Shen, M. Stable and efficient multi-crystalline n<sup>+</sup>p silicon photocathode for H<sub>2</sub> production with pyramid-like surface nanostructure and thin Al<sub>2</sub>O<sub>3</sub> protective layer. *Appl. Phys. Lett.* **2015**, *106* (1), 013902.
- (47) Fan, R.; Mao, J.; Yin, Z.; Jie, J.; Dong, W.; Fang, L.; Zheng, F.; Shen, M. Efficient and Stable Silicon Photocathodes Coated with Vertically Standing Nano-MoS<sub>2</sub> Films for Solar Hydrogen Production. *ACS Appl. Mater. Interfaces* **2017**, *9* (7), 6123–6129.
- (48) Kim, H.; Bae, H.; Bang, S. W.; Kim, S.; Lee, S. H.; Ryu, S. W.; Ha, J. S. Enhanced photoelectrochemical stability of GaN photoelectrodes by Al<sub>2</sub>O<sub>3</sub> surface passivation layer. *Opt. Express* **2019**, *27* (4), A206–A215.
- (49) Zhang, G.; Yang, D.; Sacher, E. X-ray Photoelectron Spectroscopic Analysis of Pt Nanoparticles on Highly Oriented Pyrolytic Graphite, Using Symmetric Component Line Shapes. *J. Phys. Chem. C* **2007**, *111* (2), 565–570.
- (50) Tago, T.; Kataoka, N.; Tanaka, H.; Kinoshita, K.; Kishida, S. XPS study from a clean surface of Al<sub>2</sub>O<sub>3</sub> single crystals. *Procedia Eng.* **2017**, *216*, 175–181.
- (51) Rotole, J. A.; Sherwood, P. M. A. Corundum ( $\alpha$ -Al<sub>2</sub>O<sub>3</sub>) by XPS. *Surf. Sci. Spectra* **1998**, *5* (1), 11–17.
- (52) Sadaf, S. M.; Zhao, S.; Wu, Y.; Ra, Y. H.; Liu, X.; Vanka, S.; Mi, Z. An AlGa<sub>N</sub> Core-Shell Tunnel Junction Nanowire Light-Emitting Diode Operating in the Ultraviolet-C Band. *Nano Lett.* **2017**, *17* (2), 1212–1218.
- (53) Sadaf, S. M.; Ra, Y. H.; Nguyen, H. P.; Djavid, M.; Mi, Z. Alternating-Current InGa<sub>N</sub>/Ga<sub>N</sub> Tunnel Junction Nanowire White-Light Emitting Diodes. *Nano Lett.* **2015**, *15* (10), 6696–701.
- (54) Wang, Y.; Wu, Y.; Schwartz, J.; Sung, S. H.; Hovden, R.; Mi, Z. A Single-Junction Cathodic Approach for Stable Unassisted Solar Water Splitting. *Joule* **2019**, *3* (10), 2444–2456.
- (55) He, Y.; Vanka, S.; Gao, T.; He, D.; Espano, J.; Zhao, Y.; Dong, Q.; Lang, C.; Wang, Y.; Hamann, T. W.; Mi, Z.; Wang, D. Dependence of interface energetics and kinetics on catalyst loading in a photoelectrochemical system. *Nano Res.* **2019**, *12*, 2378–2384.
- (56) Lv, C.; Chen, Z.; Chen, Z.; Zhang, B.; Qin, Y.; Huang, Z.; Zhang, C. Silicon nanowires loaded with iron phosphide for effective solar-driven hydrogen production. *J. Mater. Chem. A* **2015**, *3* (34), 17669–17675.
- (57) Chen, Z.; Jaramillo, T. F.; Deutsch, T. G.; Kleiman-Shwarscstein, A.; Forman, A. J.; Gaillard, N.; Garland, R.; Takanabe, K.; Heske, C.; Sunkara, M.; McFarland, E. W.; Domen, K.; Miller, E. L.; Turner, J. A.; Dinh, H. N. Accelerating materials development for photoelectrochemical hydrogen production: Standards for methods, definitions, and reporting protocols. *J. Mater. Res.* **2010**, *25* (1), 3–16.
- (58) Huang, G.; Mao, J.; Fan, R.; Yin, Z.; Wu, X.; Jie, J.; Kang, Z.; Shen, M. Integrated MoSe<sub>2</sub> with n<sup>+</sup>p-Si photocathodes for solar water splitting with high efficiency and stability. *Appl. Phys. Lett.* **2018**, *112* (1), 013902.
- (59) Ji, L.; McDaniel, M. D.; Wang, S. J.; Posadas, A. B.; Li, X. H.; Huang, H. Y.; Lee, J. C.; Demkov, A. A.; Bard, A. J.; Ekerdt, J. G.; Yu, E. T. A silicon-based photocathode for water reduction with an epitaxial SrTiO<sub>3</sub> protection layer and a nanostructured catalyst. *Nat. Nanotechnol.* **2015**, *10* (1), 84–90.
- (60) Fan, R.; Tang, C.; Xin, Y.; Su, X.; Wang, X.; Shen, M. Surface passivation and protection of Pt loaded multicrystalline p<sup>n</sup><sup>+</sup> silicon photocathodes by atmospheric plasma oxidation for improved solar water splitting. *Appl. Phys. Lett.* **2016**, *109* (23), 233901.
- (61) Li, L.; Wang, Y.; Vanka, S.; Mu, X.; Mi, Z.; Li, C. J. Nitrogen Photofixation over III-Nitride Nanowires Assisted by Ruthenium Clusters of Low Atomicity. *Angew. Chem., Int. Ed.* **2017**, *56* (30), 8701–8705.
- (62) Gurudayal; Sabba, D.; Kumar, M. H.; Wong, L. H.; Barber, J.; Gratzel, M.; Mathews, N. Perovskite-Hematite Tandem Cells for Efficient Overall Solar Driven Water Splitting. *Nano Lett.* **2015**, *15* (6), 3833–9.
- (63) Licht, S.; Wang, B.; Mukerji, S.; Soga, T.; Umeno, M.; Tributsch, H. Efficient Solar Water Splitting, Exemplified by RuO<sub>2</sub>-Catalyzed AlGaAs/Si Photoelectrolysis. *J. Phys. Chem. B* **2000**, *104* (38), 8920–8924.
- (64) Varadhan, P.; Fu, H. C.; Kao, Y. C.; Horng, R. H.; He, J. H. An efficient and stable photoelectrochemical system with 9% solar-to-hydrogen conversion efficiency via InGaP/GaAs double junction. *Nat. Commun.* **2019**, *10* (1), 5282.
- (65) Steiner, M. A.; Barraugh, C. D.; Aldridge, C. W.; Alvarez, I. B.; Friedman, D. J.; Ekins-Daukes, N. J.; Deutsch, T. G.; Young, J. L. Photoelectrochemical water splitting using strain-balanced multiple quantum well photovoltaic cells. *Sus. Energy Fuels* **2019**, *3* (10), 2837–2844.
- (66) Christians, J. A.; Manser, J. S.; Kamat, P. V. Best Practices in Perovskite Solar Cell Efficiency Measurements. Avoiding the Error of Making Bad Cells Look Good. *J. Phys. Chem. Lett.* **2015**, *6* (5), 852–7.
- (67) Döschner, H.; Young, J. L.; Geisz, J. F.; Turner, J. A.; Deutsch, T. G. Solar-to-hydrogen efficiency: shining light on photoelectrochemical device performance. *Energy Environ. Sci.* **2016**, *9* (1), 74–80.
- (68) May, M. M.; Lewerenz, H. J.; Lackner, D.; Dimroth, F.; Hannappel, T. Efficient direct solar-to-hydrogen conversion by in situ interface transformation of a tandem structure. *Nat. Commun.* **2015**, *6*, 8286.
- (69) May, M. M.; Lackner, D.; Ohlmann, J.; Dimroth, F.; van de Krol, R.; Hannappel, T.; Schwarzborg, K. On the benchmarking of multi-junction photoelectrochemical fuel generating devices. *Sus. Energy Fuels* **2017**, *1* (3), 492–503.
- (70) May, M. M.; Döschner, H.; Turner, J. A. Chapter 12. High-efficiency Water Splitting Systems. In *Integrated Solar Fuel Generators*; Royal Society of Chemistry, 2018; pp 454–499.
- (71) Gu, J.; Yan, Y.; Young, J. L.; Steirer, K. X.; Neale, N. R.; Turner, J. A. Water reduction by a p-GaInP<sub>2</sub> photoelectrode stabilized by an amorphous TiO<sub>2</sub> coating and a molecular cobalt catalyst. *Nat. Mater.* **2016**, *15* (4), 456–60.
- (72) Grundmann, M. J.; Mishra, U. K. Multi-color light emitting diode using polarization-induced tunnel junctions. *Phys. Status Solidi C* **2007**, *4* (7), 2830–2833.
- (73) Krishnamoorthy, S.; Nath, D. N.; Akyol, F.; Park, P. S.; Esposto, M.; Rajan, S. Polarization-engineered GaN/InGa<sub>N</sub>/Ga<sub>N</sub> tunnel diodes. *Appl. Phys. Lett.* **2010**, *97* (20), 203502.

- (74) Bernardini, F.; Fiorentini, V.; Vanderbilt, D. Spontaneous polarization and piezoelectric constants of III-V nitrides. *Phys. Rev. B: Condens. Matter Mater. Phys.* **1997**, *56* (16), R10024–R10027.
- (75) Moustakas, T. D. The role of extended defects on the performance of optoelectronic devices in nitride semiconductors. *Phys. Status Solidi A* **2013**, *210* (1), 169–174.
- (76) Li, J.; Lin, J. Y.; Jiang, H. X. Direct hydrogen gas generation by using InGaN epilayers as working electrodes. *Appl. Phys. Lett.* **2008**, *93* (16), 162107.